2021

Direct numerical simulation of a pulsatile flow in a stenotic channel using immersed boundary method

Siamak Mirfendereski

Jae Sung Park

Received: 4 March 2021 | Revised: 21 June 2021 | Accepted: 17 July 2021

DOI: 10.1002/eng2.12444

RESEARCH ARTICLE

Engineering Reports Open Access WILEY

Direct numerical simulation of a pulsatile flow in a stenotic channel using immersed boundary method

Siamak Mirfendereski | **Jae Sung Park**

Department of Mechanical and Materials Engineering, University of Nebraska-Lincoln, Lincoln, Nebraska,

Correspondence
Jae Sung Park, Department of Mechanical and Materials Engineering, University of Nebraska-Lincoln, Lincoln, NE 68588-0526, USA.
Email: jaesung.park@unl.edu

Funding information
National Science Foundation, Grant/Award Number: CBET-1936065; University of Nebraska, Grant/Award Number: Collaboration Initiative

Abstract

A three-dimensional direct numerical simulation model coupled with the immersed boundary method has been developed to simulate a pulsatile flow in a planar channel with single and double one-sided semicircular constrictions. For relevance to blood flow in large arteries, simulations have been performed at Reynolds numbers of 750 and 1000. Flow physics and resultant wall shear stress (WSS)-based hemodynamic parameters are presented. The instantaneous vortex dynamics, mean flow characteristics, and turbulent energy spectra are evaluated for flow physics. Subsequently, three WSS-based parameters, namely the time-averaged WSS, oscillatory shear index, and relative residence time, are calculated over the stenotic wall and correlated with flow physics to identify the regions prone to atherosclerotic plaque progression. Results show that the double stenotic channel leads to high-intensity and broadband turbulent characteristics downstream, promoting critical values of the WSS-based parameters in the post-stenotic areas. In addition, the inter-space area between two stenoses displays multiple strong recirculations, making this area highly prone to atherosclerosis progression. The effect of stenosis degree on the WSS-based parameters is studied up to 60% degree. As the degree of occlusion is increased, larger regions are involved with the nonphysiological ranges of the WSS-based parameters.

KEYWORDS

direct numerical simulation, flow physics, hemodynamic wall parameters, immersed-boundary method, pulsatile flow, stenotic channel

1 | INTRODUCTION

Atherosclerosis is a cardiovascular disease of mid-size and large arteries that involves narrowing the arteries and hardening of the vessel wall due to the deposition of plaque. According to the American Heart Association report in 2016, nearly half of US adults (121.5 million) have some forms of cardiovascular disease, which is consequently a chief cause of death not only in the United States both also in Europe and much of Asia.[1] As a major cause of cardiovascular disease, atherosclerosis accounts for the majority of these deaths. It is primarily a progressive inflammatory disease initiated by

a localized accumulation of low-density lipid (LDL) proteins within the artery wall, potentially resulting in atherosclerotic constriction so-called arterial stenosis. This local restriction is most common in coronary arteries, carotid arteries, and femoral arteries. From fluid dynamics and hemodynamics perspectives, the presence of constriction in the artery results in unrecoverable head loss and the reduction of blood supply. Furthermore, the high wall shear stress (WSS) at the occlusion was suggested to activate the platelet accumulation, which accelerates atherosclerosis.[2] It also may result in rapture or fissure of the plaque, which consequently leads to partial or complete thrombosis.[3] However, the formation of pathological thrombosis caused by altered hemodynamics around the plaque has yet to be understood. The thrombus formation was reported to be promoted at the outlet region of stenosis associated with stimulation of platelet aggregation and shear deceleration.[4]

Fluid dynamics in the poststenotic region is of significant importance in the development of atherosclerosis.[5] Away from the stenotic region, the poststenotic dilatation results in the disturbance in the flow field downstream, featuring separated shear layers, recirculations, reattachments, pressure fluctuation, and possibly transition to turbulence.[6-8] Accordingly, a low and oscillatory WSS around this region directly contributes to the progression of atherosclerotic plaques as the endothelial cells show an atherogenic phenotype in lesion-prone low shear stress regions[5] and the variability of WSS prevents the cells from aligning in the flow direction.[9] As a result, the endothelium at this region becomes round-shaped and more permeable to the entry of harmful constituents of blood.[10] Particularly, the low WSS was observed to contribute to the formation of plaques with vulnerable phenotype, while an oscillatory WSS induces the growth of more stabilized plaques.[11] Moreover, the low WSS and reduced blood velocity lead to increasing the resident time of atherogenic blood particles close to the arterial wall.[12] In addition to the pathological significance, fluid dynamics also plays an essential role in the diagnosis of arterial diseases, which leads to a wide range of studies to predict the severity of the stenotic occlusion[13] and to detect the localized atherosclerotic plaques.[14] In this regard, the mechanism underlying the distinct sounds produced by the blood flow in the stenotic artery, so-called arterial murmurs, is detected externally.[15]

More importantly, the unique flow characteristics at the poststenotic region may lead to the formation of the second stenosis or a series of stenoses, as the low and oscillatory WSS at this region tends to exacerbate the progression of atherosclerotic plaques and intima wall thickening.[16,17] There have been many cases in clinical observations where the patients are diagnosed with multiple sequential stenoses in one artery. Given equivalent artery length and diameter, multiple stenoses appear to impose more resistance to flow[18] and have a greater impact on blood flow[19] than single stenosis. Also, the earlier experimental study indicated that the total pressure drop across a series of stenoses is not equal to the summation of pressure drops of each stenosis, except for low Reynolds numbers when the stenoses are largely spaced.[20] Bernad et al.[21] showed the complexity in the fluid dynamic interactions between multiple stenoses in coronary arteries as the existence of one stenosis strongly affects the hydrodynamics associated with the other ones.

Computational fluid dynamics has been considered a powerful tool to study the complex fluid dynamics associated with stenosis and pulsatile flow. Lee et al.[22] used Reynolds-averaged Navier–Stokes (RANS) model and indicated that the double stenoses result in a larger area of high turbulence intensity distal to the stenoses compared with single stenosis. It is also reported that the strongest effect of the stenoses (with a 50% constriction ratio) on the flow fields arises when the space between the constrictions is four times the tube diameter for Reynolds number of 2000. It is worth mentioning that the RANS model is based on ensemble-averaged governing equations, and thus, due to its inherent limitation, it is not an ideal tool to simulate the fluid dynamics in a stenotic artery, which features pulsatile transitional flow. Direct numerical simulation (DNS), however, is the most accurate computational approach where all the spatial and temporal scales of turbulence are solved, hence it provides very accurate predictive tools. Varghese et al. and Blackburn et al. used DNS approach for steady and pulsatile flows through an axisymmetric stenosis inside a straight tube to describe the turbulence characteristics and transient growth in details.[7,23,24] Beratlis et al. used the same numerical approach for pulsatile flow through a semi-circular constriction in the planar channel, which was also validated by experimental observations from laser-Doppler velocimetry experiments.[25] Recently, the large-eddy simulation approach, where the large scales of turbulence motions are only solved and the smaller subgrid scales are modeled, has also been used in a number of studies to simulate the stenotic channels.[6,8,26,27]

In the literature, the numerical treatments of stenotic geometry in arteries have been mostly based on the boundary-fitted grids or unstructured grids. As an alternative, the immersed boundary method (IBM), which was introduced by Peskin,[28] has received much attention thanks to its less computational cost to handle the complex or even moving geometries. In this method, a simple stationary grid is employed, and then the immersed boundary is modeled by introducing a virtual force field in the domain to impose desirable boundary condition.[29,30] Note that there have been

a number of studies that used the IBM approach to develop a two-dimensional stenosis model with a rough surface.[31,32] IBM was also developed by Mittal et al.[33] to simulate the flow past three- dimensional bodies. The same IBM was later used by Seo et al.[34] for analyzing the aortic stenosis murmurs induced by the blood flow.

In general, the IBM algorithm is a promising alternative to handle complex moving boundaries,[33,35,36] and fluid–solid interaction (FSI). Moreover, it has been shown that FSI simulations seem to accurately capture flow fields over a deformable arterial wall with patient-specific geometries, whereas models based on rigid arterial walls seem to overestimate flow velocities and WSS values.[37,38] Therefore, an FSI model has been used to simulate a patient-specific pulmonary artery,[39] aortic dissection,[40] coronary artery,[37] and carotid artery.[41] Specifically, Liu et al. used MRI (magnetic resonance imaging) data to construct the input geometry and captured the vessel wall deformation following hyper-elastic constitutive law.[42] In this regard, an IBM-based model has also been developed to simulate a blood flow in complex geometries, particularly arterial blood flow.[33,43] For instance, Chen et al. employed a sharp-interface IBM to simulate the hemodynamics in the realistic geometry of carotid arteries.[43]

It appears that the previous studies on blood flow over multiple stenoses are mostly limited to the overall features of fluid flow, for example, pressure drop and mean flow pattern. Although the presence of multiple stenoses has been reported to potentially increase the overall pressure drop, there have been limited studies to show a detailed investigation on this observation in terms of temporal flow structures. In addition, the evaluation of WSS-based hemodynamic parameters is generally lacking in the previous studies that mainly focused on a discussion of the constricted flow features, such as turbulence characteristics. To our knowledge, there is a very limited study on coupling the constricted flow features with the resultant WSS-based quantities to relate them to the atherosclerosis progression, especially with multiple constrictions.

In the present study, we develop a DNS model based on the finite-difference algorithm coupled with the IBM to simulate a pulsatile flow in a three-dimensional channel with one-sided semi-circular stenotic geometry. Here, we aim to characterize a turbulent fluid flow in single and double occlusions and the resultant WSS pattern to correlate the flow features to atherosclerosis progression. Although the simplified stenotic geometries are used for occlusion in the present model, they have been widely employed in numerous computational studies to characterize a constricted fluid flow for stenotic arteries and provide important insights into flow physics.[6,8,24,25,44] However, it should also be noted that an IBM-based DNS model has a potential to simulate more realistic vessel walls such as patient-specific geometries and hyper-elastic walls, which is beyond the scope of the current study and should motivate future work. In the following sections, we present both instantaneous and mean flow characteristics for single and double constricted channels at Reynolds numbers of 750 and 1000 reported to be within the range of the characteristics of the blood flow in human large arteries.[6,8] Furthermore, the WSS-based descriptors are determined over the stenotic wall surfaces at various degrees of stenosis for single and double stenoses. An insight into the critical regions prone to the formation of atherosclerotic plaque is discussed.

2 | PROBLEM FORMULATION

To simulate a flow over stenotic arteries, we consider an incompressible Newtonian flow in a planar channel with one or two semicircular constrictions on its bottom wall, as seen in Figure 1. A channel with a single constriction was similar to the geometry previously simulated by Mittal et al.[6,26] Note that x, y, and z refer to the streamwise, wall-normal, and spanwise directions, respectively, where the corresponding velocities are u, v, and w, respectively. To incorporate a constriction in a flow, we use the IBM with a ɛdirect forcing approachɛ to impose no-slip boundary conditions at the solid boundaries, which are the surface of the constrictions in the present study. This method is recognized as a powerful tool to effectively handle complex geometries even with severe irregularities.[31,32] The nondimensional governing equations for an unsteady incompressible fluid flow are then written as follows

$$\nabla \cdot \boldsymbol{u} = 0. \tag{1}$$

$$\frac{\partial \boldsymbol{u}}{\partial t} + \boldsymbol{u} \cdot \nabla \boldsymbol{u} = -\nabla p + \frac{1}{Re}\nabla^2 \boldsymbol{u} + \boldsymbol{f}. \tag{2}$$

Here, the Reynolds number is defined as $Re = Uh/\nu$, where h denotes channel height and U is the peak inflow bulk velocity. The virtual force vector field $\boldsymbol{f}$, which is referred to as an IBM direct-forcing term, is specified to impose the

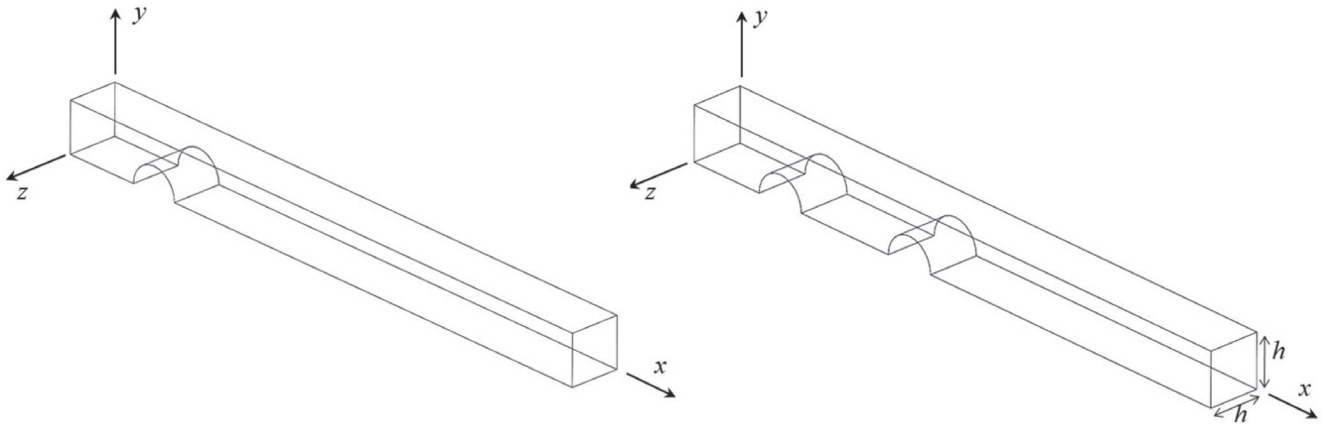

FIGURE 1 Schematic of the channels with one-sided semi-circular geometry of single constriction (left) and double constrictions (right)

no-slip boundary condition on solid surfaces or stenotic surfaces. This approach results in gradual attainment of the desired value of velocity on the boundary during every time-stepping computation without any dynamical process.[29] A general approach of IBM is to initially generate a simple stationary mesh in the simulation domain without including any immersed bodies such as constrictions and then introduce a source term into the Navier–Stokes equations to enforce specified boundary conditions over the immersed boundaries. The main advantage of this approach is that the source term can be prescribed on a regular Cartesian mesh by which the efficiency and accuracy of the computation process can be maintained. In addition, a wide variety of boundary shapes can be included in the simulation thanks to the inherent ability of IBM to deal with these complex boundaries without the significant necessity of compromising the regular stationary mesh.

2.1 | Numerical method

In the present model, which is based on the DNS, we couple the direct forcing approach of IBM with the finite difference method to solve Equations (1) and (2). Similarly, Fadlun et al.[29] and Kim et al.[30] developed IBM with a direct forcing approach for finite-difference and finite-volume methods in a three-dimensional complex flow, respectively. Here, a fractional step algorithm, or time-split method, is employed on a staggered mesh. A three-step time-splitting scheme is used to compute a fluid field. On the first step, given the velocity $\boldsymbol{u}^n$ at the current time step n, an intermediate velocity $\boldsymbol{u}^*$ is introduced and calculated by implementing the second-order Adams–Bashforth scheme for temporal discretization as

$$\frac{\boldsymbol{u}^* - \boldsymbol{u}^n}{\Delta t} = \frac{3}{2}\boldsymbol{F}^n - \frac{1}{2}\boldsymbol{F}^{n-1}, \tag{3}$$

where $\boldsymbol{F} = -\boldsymbol{u}\cdot\nabla\boldsymbol{u} + 1/Re\nabla^2\boldsymbol{u}$ that includes the convective and diffusive terms of the momentum equation in Equation (2). On the second step, the intermediate velocity is then corrected by a pressure gradient as follows:

$$\frac{\boldsymbol{u}^{**} - \boldsymbol{u}^*}{\Delta t} = -\nabla p^{n+1}, \tag{4}$$

where $\boldsymbol{u}^{**}$ is the second intermediate velocity and satisfies the continuity such that $\nabla\cdot\boldsymbol{u}^{**} = 0$. By applying the continuity $\nabla\cdot\boldsymbol{u}^{**} = 0$ to Equation (4), the following Poisson equation can be derived:

$$\nabla^2 p^{n+1} = \frac{1}{\Delta t}\nabla\cdot\boldsymbol{u}^*. \tag{5}$$

Once the pressure field is obtained by solving the above Poisson equation using the successive over-relaxation method, the second intermediate velocity can be readily advanced by Equation (4). On the third step, the source term $\boldsymbol{f}^{n+1}$ is

explicitly computed at the grid points located inside the immersed body to update the velocity field to the next time step $n+1$ by the following equation

$$\frac{\boldsymbol{u}^{n+1}-\boldsymbol{u}^{**}}{\Delta t}=\boldsymbol{f}^{n+1}, \tag{6}$$

where the virtual force term $\boldsymbol{f}$ should be determined for the action of solid upon a fluid to satisfy the no-slip boundary on the solid surface. Specifically, the force term is zero within the fluid domain and nonzero on the solid body, where it is proportional to the difference between the prescribed solid velocity and the fluid velocity. It can be simply expressed as

$$\boldsymbol{f}^{n+1}=\eta\frac{\boldsymbol{u}_s^{n+1}-\boldsymbol{u}^{**}}{\Delta t}, \tag{7}$$

where $\boldsymbol{u}_s$ is the prescribed velocity of the solid body and η is the prefactor to decide solid and fluid sides. The prescribed velocity should be equal to zero if the solid body is stationary, which is the case for the current study. For any grid points inside the solid body, $\eta=1$, indicating the solid cells; otherwise, $\eta=0$, representing the fluid cells. Moreover, we implement a linear interpolation to impose the desired condition right at the boundary surface points.

2.2 | Flow configuration

The geometry of the three-dimensional channels with one and two stenoses in the current simulations is depicted in Figure 1. We choose a similar model of stenotic arteries to that used by Mittal et al.,[6,26] Tutty et al.,[45] and Griffith et al.[46] As seen in the figure, the computational domain consists of single or double semi-circular constrictions on the bottom wall of the planar channel. The stenosis in the single constricted channel and the proximal (first) stenosis in the double constricted channel are centered at $x/h=10$. The distal (second) stenosis in the double constricted channel is centered at $x/h=13$. The channels extend $20h$ and h in the streamwise and spanwise directions, respectively.

It has been reported that the physiological waveforms of an arterial flow are not sinusoidal and essentially depend upon the blood vessel.[19] However, a number of studies have shown that the pressure gradient can be approximated as temporal Fourier series:

$$\frac{\partial p}{\partial y}=A_0+\sum_{n=1}^{N}A_n e^{in2\pi\Omega t+\varphi_n}, \tag{8}$$

where A_0 and A_n take steady and oscillatory parts of pressures gradient, respectively. In the summation of Equation (8), the Strouhal number $\Omega=h/TU_b$ represents the nondimensional frequency of pulsation at the inlet flow, where T is the time period of the pulsation and U_b is the bulk velocity at the peak inflow, and φ_n represents the phase angle.[8,27] In the current study, we intend to include a leading term of the oscillatory part in the pressure gradient (see Equation (8)) as similar to some experimental and numerical studies.[6,32,47] The following sinusoidal waveform is now considered as a simple prototype of physiological waveforms:

$$\frac{\partial p}{\partial y}=A_0+A_1 e^{i2\pi\Omega t}. \tag{9}$$

In addition, we employ the velocity profile corresponding to the laminar fully developed pulsatile flow in the planar channel as an inflow condition. The inflow velocity profile is then the solution of the following equation, where right-hand side indicates the pressure gradient in Equation (9)

$$\frac{\partial u}{\partial t}-\frac{1}{Re}\frac{\partial^2 u}{\partial y^2}=-A_0-A_1 e^{i2\pi\Omega t}. \tag{10}$$

This equation indeed has the following analytical solution:

$$u(y,t)=\frac{3}{4}\left[1-\left(\frac{y-h/2}{h/2}\right)^2\right]-i\left[1-\frac{\cosh(2\alpha\sqrt{i}(y-h/2))}{\cosh(\alpha\sqrt{ih})}\right]f e^{i2\pi\Omega t}. \tag{11}$$

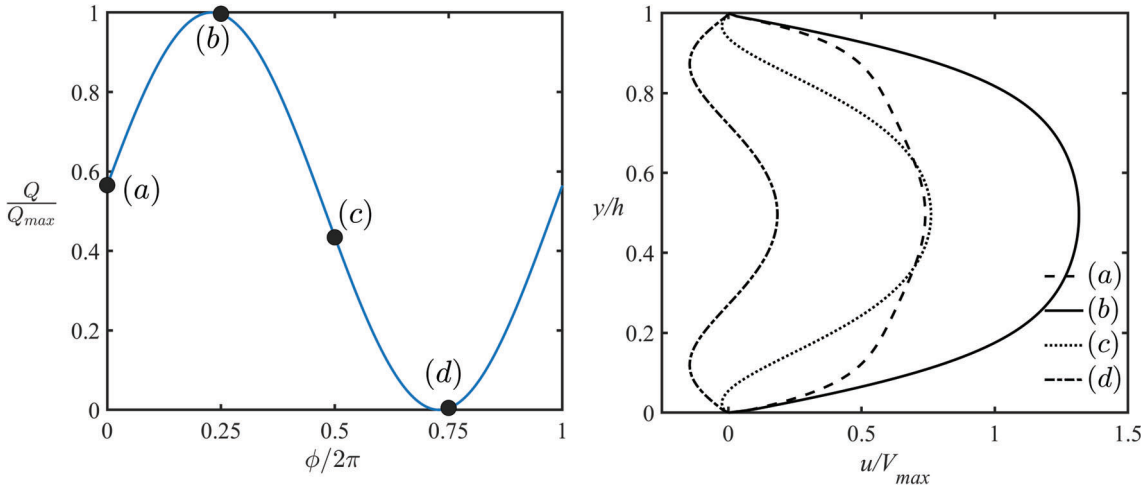

FIGURE 2 (Left) Temporal variation of an inlet volume flow rate normalized by its maximum value. Four different pulsatile phases are indicated. (Right) Inflow velocity profiles for $\alpha = 6.1$ at $Re = 1000$ based on Equation (11)

The real part of the above solution provides the streamwise velocity profile for the inlet boundary condition. In the solution, there is Womersley number $\alpha = \sqrt{\pi Re\Omega/2}$, which reflects the ratio of the pulsatile inertial forces to the viscous forces.[8] The Womersley number has been widely used to describe cardiovascular flows.[19] The shape of the inlet velocity profile depends upon the Womersley number, where $\alpha = 5.3$ and 6.1 for $Re = 750$ and 1000, respectively, at the fixed frequency of pulsation. The coefficient f is seen to be a function of α, which is determined to match the volume flux condition.[6,26] Typically, it is set to change within the range of $[0, 1]$. Figure 2(A), (B) shows the normalized volumetric flow rate over one pulsatile cycle and the inflow velocity profiles at four sequential phases in a pulsatile cycle, respectively. Note that the phase ϕ is equal to $2\pi t/T$. For the outflow boundary, a convective boundary condition is applied at $x/h = 20$, and the periodic boundary condition is applied on the spanwise boundaries. No-slip boundary condition is imposed at the wall locations $y = 0$ and $y = h$.

2.3 | Data reduction

In order to define the averaging operations, we use the data processing methods similar to those used by Molla et al.,[27] Varghese et al.,[7] and Mittal et al.[6] For a generic flow variable g, the average over a period time of N cycles and the spanwise direction is computed as follows:

$$\langle g\rangle(x,y) = \frac{1}{L_z}\frac{1}{NT}\int_{t_0}^{t_0+NT}\int_0^{L_z} g(x,y,z,t)dzdt, \tag{12}$$

where t_0 is the beginning time of the time-averaging process and L_z indicates the domain size in the spanwise direction. The deviation from the averaged value is then computed as

$$g' = g - \langle g\rangle. \tag{13}$$

The time-varying coherent part of flow variable g in response to pulsation can be determined by making phase average over N cycles as

$$\tilde{g}(x,y,t) = \frac{1}{L_z}\frac{1}{N}\sum_{n=0}^{N-1}\int_0^{L_z} g(x,y,z,t+nT)dzdt. \tag{14}$$

The deviation from the phase average $\tilde{g}$ is then computed by

$$g'' = g - \tilde{g}, \tag{15}$$

which represents a nondeterministic part of flow and turbulence characteristics.

3 | RESULTS AND DISCUSSION

The simulation results for Reynolds numbers of 750 and 1000, and Strouhal number of 0.0239 are presented. These parameters are consistent with typical characteristics of blood flow inside large arteries.[48] The grid system of $N_x \times N_y \times N_z = 640 \times 128 \times 32$ and a nondimensional time step in the range of $2.5 \times 10^{-4} - 5 \times 10^{-4}$ are used to ensure stabilization of the current simulations. Before selecting this gird system, we have examined the grid independence for Reynolds number of 1000 to ensure that the velocity field and WSS are insensitive to the grid resolution. Specifically, we have tested the grid resolution using different cell numbers in the streamwise, wall-normal, and spanwise directions, namely, $N_x = 640 - 960$, $N_y = 128 - 196$, $N_z = 32 - 48$, respectively, all of which provide identical results.

Firstly, we validate the numerical model developed. Secondly, we characterize the fluid dynamics associated with the presence of one and two constrictions in a planar channel. Thirdly, we evaluate the WSS-based descriptors, including time-averaged WSS (TAWSS), oscillatory shear index (OSI), and relative residence time (RRT), all of which can lead to characterizing the progression of atherosclerotic plaque. These descriptors will be evaluated at different degrees of stenosis and for single and double stenoses.

3.1 | Validation

The accuracy of the current numerical model has been examined with the results of Mittal et al.,[6] where a similar one-sided semi-circular geometry of constriction with a 50% reduction in channel area was simulated. The skin friction coefficients $\langle C_f \rangle$ on the upper and lower walls are defined by $\langle C_f \rangle = 2\langle \tau_w \rangle / \rho U^2$, where τ_w denotes the WSS. Note that τ_w is calculated over the bottom wall at the upstream and the downstream of the constriction as well as over the surface of the semi-circular stenotic area ($9.5 < x/h < 10.5$). In Section 3.3, τ_w across the channel is calculated in a similar fashion. The variation of skin friction with the streamwise direction (x) on both walls at Reynolds number of 750 is presented in Figure 3. Note that the WSS is ensemble-averaged over the period of nine pulsatile cycles and the spanwise direction. As seen in the figure, the skin friction coefficient at both lower and upper walls from the current calculation is in excellent agreement with that in Mittal et al.[6] Particularly, the location and the magnitude of peak values in the skin friction coefficient curves are almost identical. It is worth noting that the locations of the maximum value of the skin friction coefficient are close to the lip of constriction, which is associated with a high mean streamwise velocity. There is also a region with negative WSS downstream of the constriction due to the strong localized recirculation. In addition, the crinkles in the skin friction coefficient curve further downstream can be explained as an indication of the separation and reattachment process in shear layers, which was also observed by Mittal et al.[6]

3.2 | Flow physics

3.2.1 | Vortex dynamics

To characterize the instantaneous fluid dynamic behaviors in both single and double stenotic channels, we compute the magnitude of the spanwise vorticity ($\omega_z = \partial v/\partial x - \partial u/\partial y$) averaged over the spanwise direction. Indeed, the spanwise

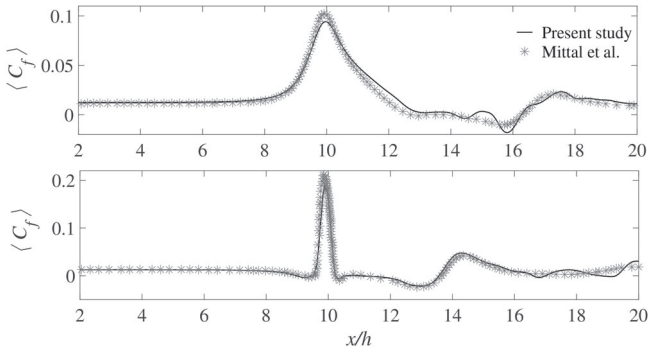

FIGURE 3 The comparison of the mean skin friction coefficient $\langle C_f \rangle = 2\langle \tau_w \rangle / \rho U^2$ with that of Mittal et al.[6] at the top wall (top) and the bottom wall (bottom)

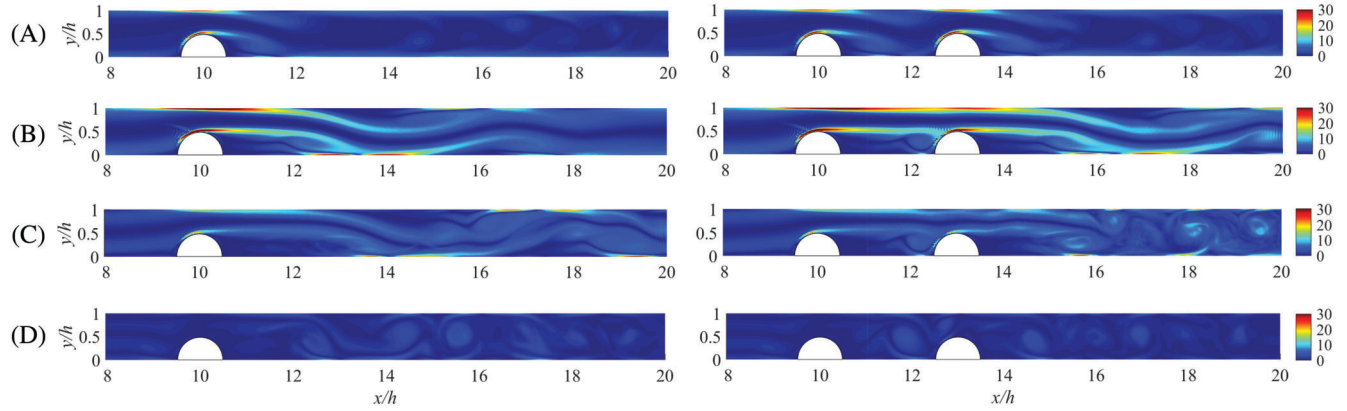

FIGURE 4 (Color online) The sequence of the spanwise-averaged spanwise vorticity ω_z for $Re = 750$ in single and double stenotic channels at four pulsatile phases indicated in Figure 2: (A) $\phi = 0$, (B) $\phi = \pi/2$, (C) $\phi = \pi$, and (D) $\phi = 3\pi/2$. Also see the accompanying Videos S1 and S2

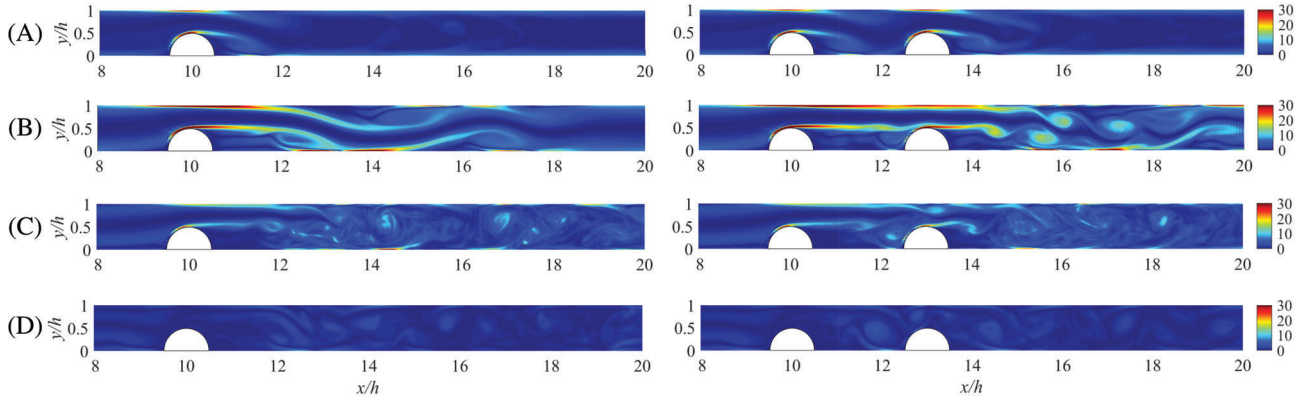

FIGURE 5 (Color online) The sequence of the spanwise-averaged spanwise vorticity ω_z for $Re = 1000$ in single and double stenotic channels at four pulsatile phases indicated in Figure 2: (A) $\phi = 0$, (B) $\phi = \pi/2$, (C) $\phi = \pi$, and (D) $\phi = 3\pi/2$. Also see the accompanying Videos S3 and S4

vorticity can illustrate the formation mechanism of the shear layers and interactions with the boundaries, and the transition to turbulence. Four different phases of the pulsatile cycle are considered as indicated in Figure 2. Figures 4 and 5 show the contour of the spanwise vorticity in the single (left column) and double (right column) stenotic channel at Reynolds numbers of 750 and 1000, respectively.

For $Re = 750$, Figure 4(A) shows the spanwise-averaged ω_z at the phase of pulsation at which the accelerating inflow rate is approximately 56% of the maximum. No significant differences are seen in the poststenotic region between the single and double stenotic channels. The clockwise rotating vortex is observed right after the stenosis in the single stenotic channel, which is created by rolling down the shear layer detached from the lip of the constriction. This vortex is almost identical to that in the double stenotic channel. The formation of these so-called shear layers, which can be tracked by the regions with higher vorticity magnitude,[6,7,23] is the consequence of the rapid increase in velocity due to the area reduction in the stenotic region. The subsequent separation of the shear layers from the lip of the constrictions is the result of an adverse pressure gradient via the increasing effective area in the outlet region of the constriction. This area reduction also induces a shear layer at the upper wall of the stenotic region, which subsequently detaches from the wall.

Figure 4(B) shows the phase of the maximum flow rate. For both single and double stenotic channels, the vortical structures are extended further downstream and other shear layers are formed at the bottom wall. For the double stenoses, a shear layer induced from the first (proximal) stenosis detaches itself from the stenosis lip and then reaches the second (distal) stenosis, which causes the part of the shear layer to roll down and creates a rotating vortex. This seemingly

strong vortex appears to persist quite a while during the pulsatile cycle as it is also indicated in the next two phases. In the poststenotic region, however, there is no significant difference in the vortical pattern of the single and double stenotic channels. It is worth noting that the presence of additional constriction slightly increases the disturbance in the vortical structure of the post-stenotic region. Figure 4(C) shows the phase associated with the decelerating mean flow rate of approximately 42% of the maximum value. At this phase, the flow field appears to be the least ordered at the poststenotic region compared to the other three phases. In addition, the effect of the double stenoses on the flow field is noticeable as a significant enhancement of vortex structures and mixing is observed downstream compared to the single stenotic channel. Figure 4(D) corresponds to the phase at which the mean inflow rate is approximately equal to zero. An array of vortex structures in the poststenotic region seems to persist, indicating no sign of relaminarization during the deceleration phase. Additionally, the rotating vortex in the area between the constrictions ($10 < x/h < 13$) is still noticeable, spanning nearly the whole channel. See the accompanying Videos S1 and S2 showing the aforementioned evolution of the spanwise vorticity during six pulsatile cycles. For $Re = 1000$, Figure 5 shows the sequence of the magnitude of the spanwise-averaged spanwise vorticity. Figure 5(A) shows the first pulsatile phase, where the vortex dynamics in both channels is quite similar to that of $Re = 750$. In the next phase corresponded to the maximum flow rate (Figure 5(B)), the vortex dynamics of the post-stenotic region of the channel with a single constriction is also similar to that at $Re = 750$. However, a dramatic change in the flow field and vortex structures is observed downstream for the double stenotic channel compared to that for the single constricted channel, as opposed to the case of $Re = 750$. As seen in the contour of the double stenotic channel, the strong shear layers from the upper and lower walls at the stenotic region around the distal stenosis appear to break into vortex shedding structures, moving towards the channel outlet. This vortex shedding phenomenon in the poststenotic region was previously seen by Varghese et al.,[23] Lieber & Gidden[49] and Ahmed and Gidden.[47] In the next phase shown in Figure 5(C), the generated vortices appear to disintegrate further into a large number of smaller-scale vortical structures in the poststenotic region, leading to the least ordered vortex pattern compared to the other three pulsatile phases. In addition, the poststenotic flow of this phase is associated with stronger disturbance in comparison to that at the lower Reynolds number. However, the presence of additional constriction upstream leads to a further increase in the poststenotic disturbance as it also does for the lower Reynolds number at this particular pulsatile phase. Figure 5(D) shows the final phase at which the mean flow rate becomes almost zero, where the fluid field is qualitatively similar to the lower Reynolds number. See the accompanying Videos S3 and S4 showing the aforementioned evolution of the spanwise vorticity during six pulsatile cycles.

3.2.2 | Mean flow feature

In order to characterize the mean flow, the mean streamlines are calculated by the spanwise- and time-averaged velocity components ($\langle u \rangle, \langle v \rangle$). Figures 6 and 7 show the the mean streamlines at $Re = 750$ and 1000 for the single and double stenotic channels, respectively. The color contour represents the magnitude of the mean velocity projected in the $x - y$ plane. At $Re = 750$, both single and double stenotic channels display a large recirculation region close to the lower wall in the immediate poststenotic region as shown in Figure 6. This recirculation region is associated with a flow reversal and low and oscillatory WSS, consequently leading to a possible increase in the residence time of blood constituents. Therefore, this region should be of significant importance in the progression of atherosclerotic plaque, which is further

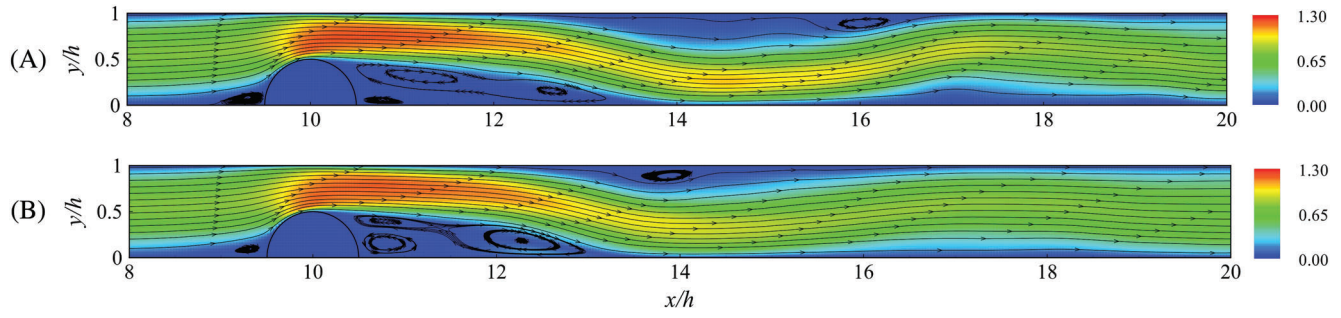

FIGURE 6 (Color online) The mean streamlines in the $x - y$ plane calculated by the spanwise- and time-averaged velocity components ($\langle u \rangle, \langle v \rangle$) for the single stenotic channel at (A) $Re = 750$ and (B) $Re = 1000$. The color contour represents the magnitude of the mean velocity

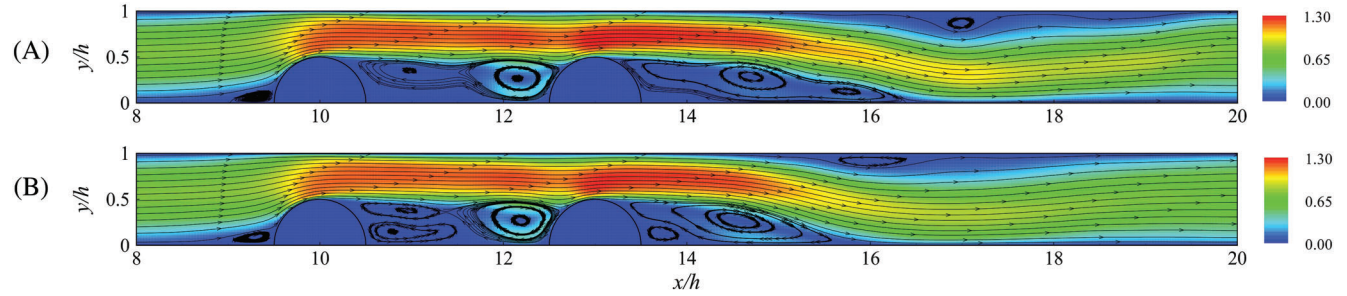

FIGURE 7 (Color online) The mean streamlines in the $x - y$ plane calculated by the spanwise- and time-averaged velocity components ($\langle u \rangle, \langle v \rangle$) for the double stenotic channel at (A) $Re = 750$ and (B) $Re = 1000$. The color contour represents the magnitude of the mean velocity

discussed in Section 3.3. This recirculation region extends in the x direction about $3.5h$ from the peak of the stenosis for $Re = 750$, similar to that of Mittalet al.,[6] and about $3h$ for $Re = 1000$. The decrease in the extent of the recirculation region for a higher Reynolds number is due to the faster rolling down of the shear layer separated from the lip of the constriction. In addition, the higher magnitude of the mean velocity at the edges of the mean recirculation region is seen for $Re = 1000$ compared with that for $Re = 750$, which suggests that the higher Reynolds number leads to the stronger recirculation.

Figure 7 shows the effect of an additional constriction on the mean flow. Depending on the Reynolds number, one or two recirculation regions are immediately formed right after the proximal stenosis followed by a stronger recirculation region before the distal stenosis. This stronger recirculation region extends in the x and y direction about $1.125h$ and $0.45h$, respectively. The long-lasting, strong recirculation between the two constrictions is believed to be of pathological significance and associated with the critical location of the bottom wall at which the atherosclerotic plaque is consequently more likely to develop. As the Reynolds number increases, the recirculation zones tend to strengthen, and the recirculation region close to the proximal stenosis breaks into two smaller counter-rotating ones. Moreover, the recirculation zone after the distal stenosis for both Reynolds numbers seems to be stronger due to the higher velocity magnitude around its edges. It suggests that the presence of an additional constriction strengthens the recirculation in the poststenotic region.

3.2.3 | Turbulent statistics

To ensure turbulent features, we calculate the turbulent kinetic energy in the streamwise direction, which is defined as $\langle u''u'' \rangle/2$. The contours of turbulent kinetic energy in the streamwise direction are shown in Figure 8. Firstly, it is clearly seen that the intensity of turbulence increases with Reynolds number for both single and double constricted channels. It is likely due to an increase in instability and consequently further generation and breakup of the vortices as the Reynolds number is increased. These vortices are primarily emanated from the separated shear layer as discussed in Section 3.2.1. Secondly, Figure 8 shows that the post-stenotic flow of the double constricted channel displays a significantly stronger turbulent intensity. It is also seen that the region of the high turbulent fluctuation intensity gets much closer to the constriction in the double constricted case.

To further analyze turbulent characteristics, we calculated the nondimensional energy spectra $E_{u''u''} = E(f_f)U/h$ of the streamwise velocity fluctuation, as seen in Figures 9 and 10 for Reynolds numbers of 750 and 1000, respectively. Note that nondimensional Strouhal number for a fluctuating flow is defined as $Sr = f_f h/U$, where f_f is the fluctuation frequency. The energy spectra were calculated at the streamwise locations of $x = 14h$ and $x = 17h$ for single and double stenotic channels, respectively. These locations correspond to $3h$ downstream of the second occlusion in the double constricted channel and $3h$ downstream of the constriction in the single constricted channel. A wall-normal location $y = 0.1h$ away from the bottom wall was used. The current spectra analysis is similar to ones in Mittal et al.[6] and Varghese et al.[7] For all cases, it is clearly seen that the inertial subrange follows the well-known scale of $\sim Sr^{-5/3}$, where the inertial transfer is dominated and the energy is cascaded from the large to small eddies due to viscous dissipation. As observed by the previous studies,[6,7,50] the second scale is found as $\sim Sr^{-10/3}$, which shows evidence that such scale results from a post-stenotic flow. It is worth noting that Lu et al.[51] observed the same spectra slope change from $-5/3$ to $-10/3$ at a distinct frequency, which could be linked to the arterial murmur.

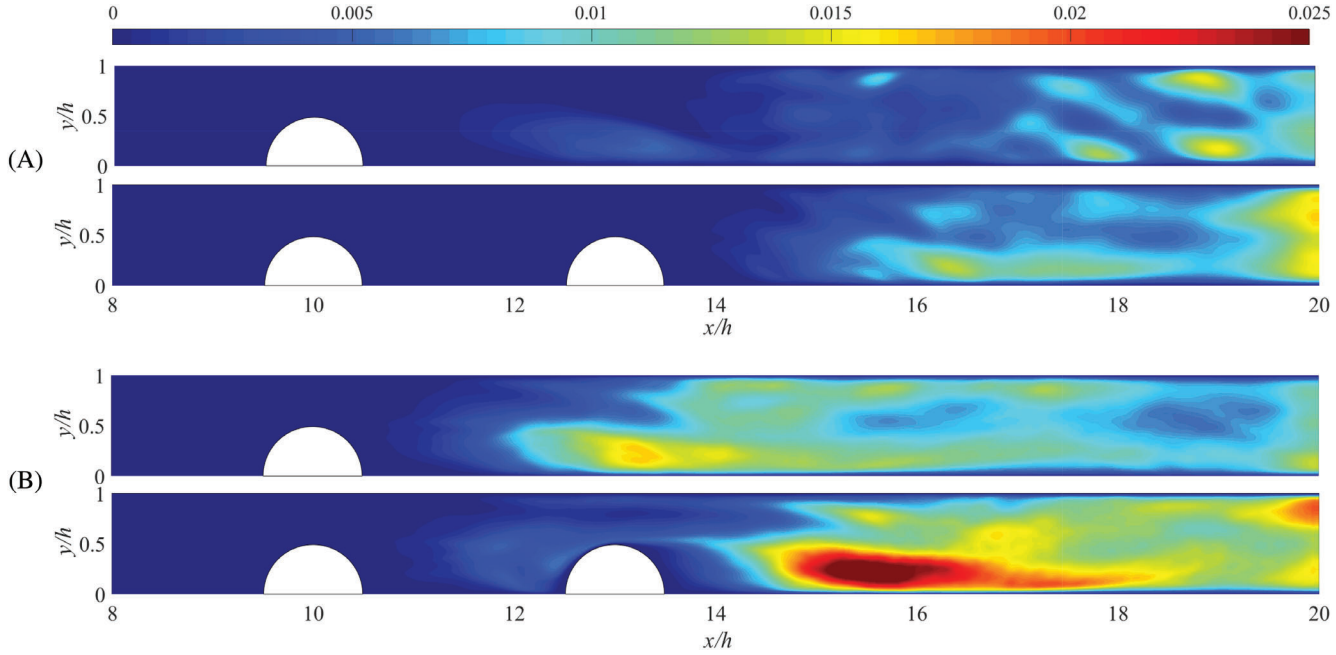

FIGURE 8 (Color online) Turbulent kinetic energy $\langle u''u'' \rangle/2$ in the streamwise direction for (A) $Re = 750$ and (B) $Re = 1000$ in the single and double constricted channels

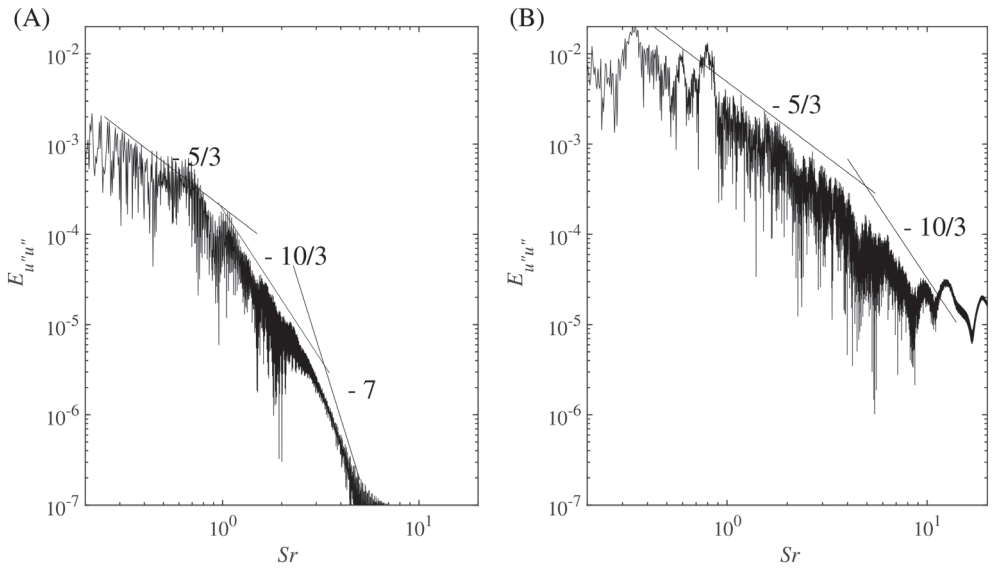

FIGURE 9 Energy spectra of the streamwise fluctuation u'' at $Re = 750$ for (A) single and (B) double stenotic channels. The streamwise location is $3h$ downstream of the stenosis, which corresponds to $x = 14h$, and $x = 17h$ for single and double constricted channels, respectively. The wall-normal distance is $y = 0.1h$ from the bottom wall

Interestingly, there is a distinct difference between the single and double constricted channels beyond the second scale of $\sim Sr^{-10/3}$. While the double constricted channel continues to show the second scale up to high frequencies, the single constricted channel exhibits the third scale of $\sim Sr^{-7}$ at a high frequency, which has also been observed in the previous studies by Mittal et al.[6] and Varghese et al.[7] This much steeper slope characterizes the dissipation range, where viscous stress becomes predominant. This third scale seems to be observed only for the single stenotic channel. Another interesting observation is a frequency at which there is a transition from $\sim Sr^{-5/3}$ to $\sim Sr^{-10/3}$. As seen in the energy spectra at both $Re = 750$ and $Re = 1000$, the double constricted channel falls to the second scale of $\sim Sr^{-10/3}$ at a much higher

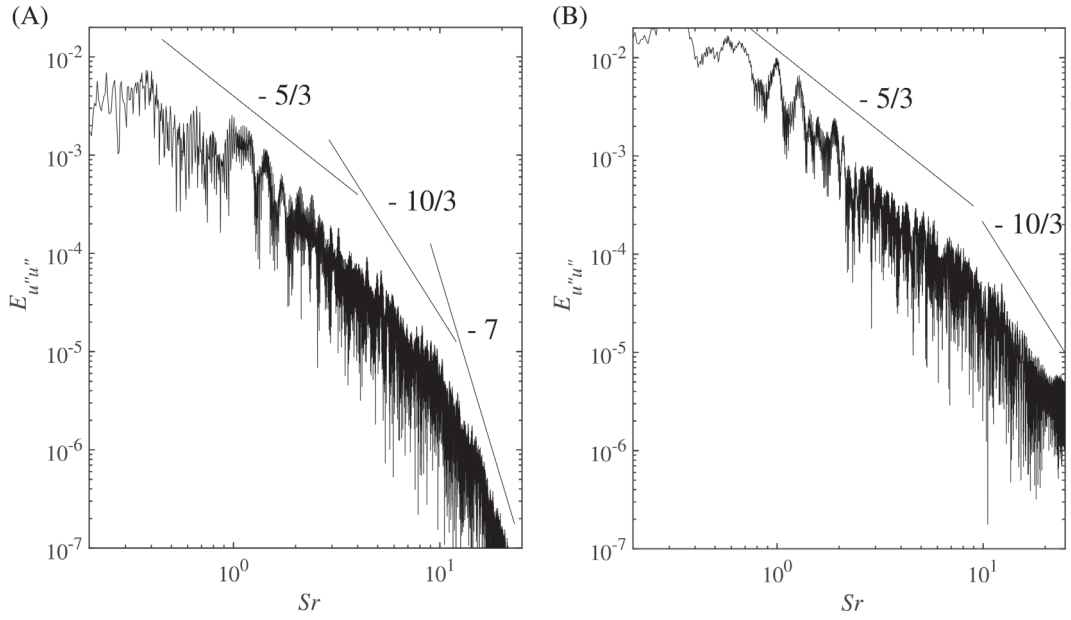

FIGURE 10 Energy spectra of the streamwise fluctuation u'' at $Re = 1000$ for (A) single and (B) double stenotic channels. The streamwise location is $3h$ downstream of the stenosis, which corresponds to $x = 14h$, and $x = 17h$ for single and double constricted channels, respectively. The wall-normal distance is $y = 0.1h$ from the bottom wall

frequency than the single constricted channel, which indicates a larger range of frequencies in the inertial subrange. This broadband nature of the inertial subrange is also referred to as fairly well-developed turbulence indicative of the dominance of the inertial effect[7].

3.3 | WSS-based hemodynamics

Now we aim at quantifying hemodynamics over single and double stenotic flows, which potentially predicts the vascular wall malfunction. In this regard, a variety of hemodynamic wall parameters has been proposed and used.[11,52,53] In particular, the hemodynamic WSS provides an important insight into the pathogenesis of atherosclerosis, which leads to cellular and molecular investigations of the endothelium's response to the shear stress.[5,54,55] To that end, three WSS-based descriptors including the time-averaged WSS (TAWSS), oscillatory shear index (OSI), and relative residence time (RRT) are evaluated in the presented study.

The TAWSS is calculated by the following equation to quantify the average characterization of the WSS over the overall pulsatile cycle T,

$$\mathrm{TAWSS} = \frac{1}{T}\int_0^T |\tau_w| dt, \tag{16}$$

where τ_w is the total arterial WSS, which is known as an essential parameter to locate early atherosclerosis.[52,56] Particularly, the low arterial hemodynamic WSS has been seen to transform the morphology of the endothelial cells into cobblestone-shaped and their configuration into random orientation.[5] In addition, the low WSS (< 0.4 Pa) has been reported to contribute to the functional switching to atherogenic endothelial phenotype, while the relatively high shear stress for physiological arterial levels (> 1.5 Pa) induces atheroprotective phenotype.[5] As the localization of the atherosclerotic plaque is associated with an oscillatory WSS,[9,10,57] the OSI is known as an index for the axial directional change of τ_w to quantify the amplitude of the WSS oscillation.[58] The OSI is defined as

$$\mathrm{OSI} = \frac{1}{2}\left(\frac{1 - \left|\int_0^T \tau_w\right|}{\int_0^T |\tau_w|}\right), \tag{17}$$

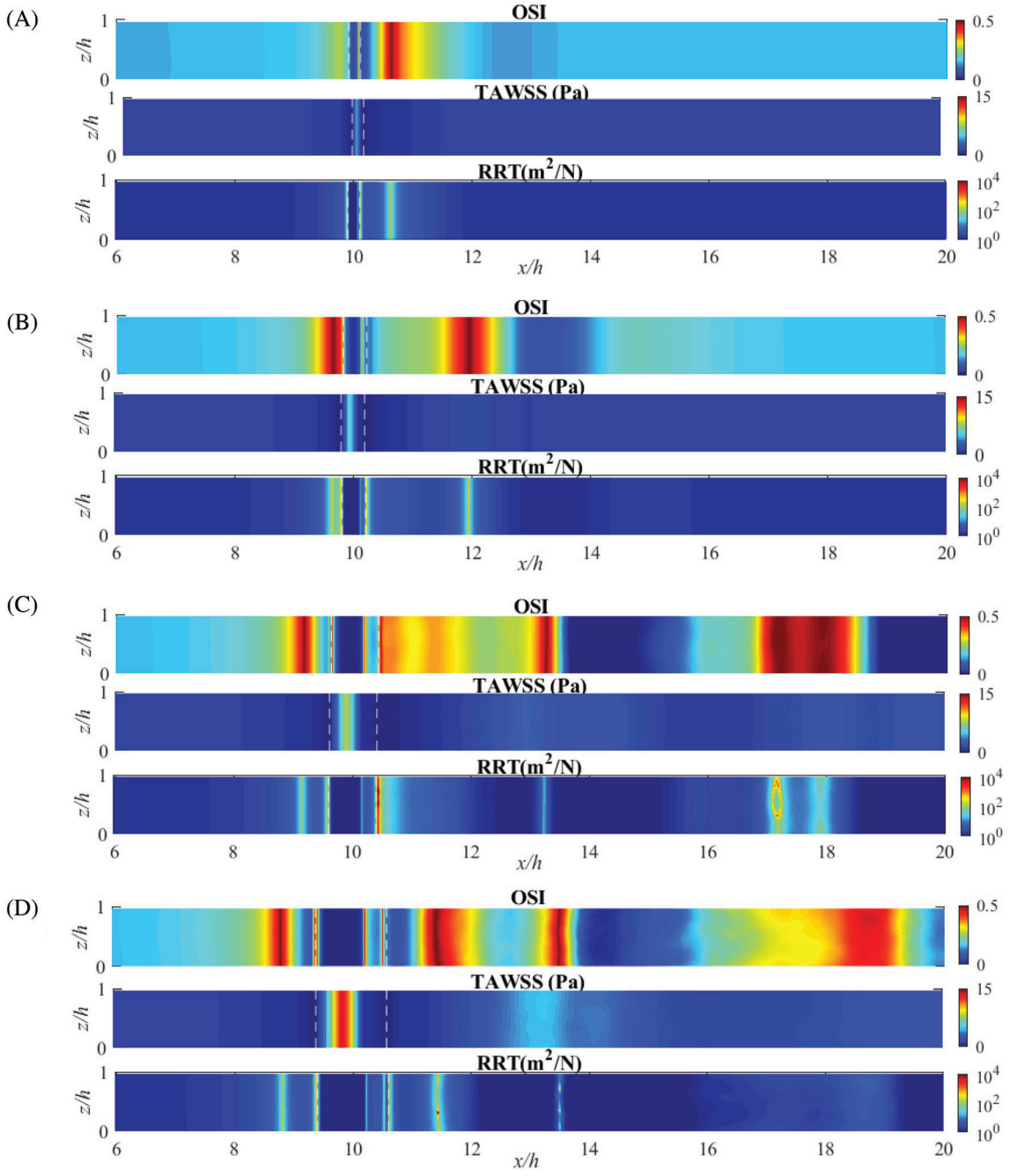

FIGURE 11 (Color online) (A) Wall shear stress-based descriptors including the time-averaged wall shear stress (TAWSS), oscillatory shear index (OSI) and relative residence time (RRT) at $Re = 750$ for a single stenotic channel with the degree of stenosis of (A) 10%, (B) 20%, (C) 40%, and (D) 60%. The dashed lines indicate the edges of the stenosis centered at $x/h = 10$. Note that the size of stenosis grows as the level of stenosis increases

where it ranges from 0 being the unidirectional shear to 0.5 being the oscillatory shear. The OSI has been considered as a useful WSS-based descriptor to diagnose arterial diseases as it can predict the regions prone to the development of the plaque.[52,57] However, one drawback to the OSI is its incapability to account for the magnitude of the WSS. With that said, RRT may fill this gap as it is a function of both magnitude and oscillation of WSS. Particularly, it is inversely proportional to $(1 - 2 \times \text{OSI})$ and TAWSS.[9,59,60] Thus, the RRT value is calculated as,

$$\text{RRT} = \frac{1}{(1 - 2 \times \text{OSI}) \times \text{TAWSS}}, \tag{18}$$

where it ranges between 0 and infinite. The RRT values higher than 8 have been considered as a critical range.[61] Note that RRT indicates the residence time of the atherogenic particles such as LDL near the vessel wall.[9] To evaluate these three WSS-based indexes, we incorporate the typical blood properties in large human arteries.[62] Therefore, the blood is assumed to be Newtonian, and the dynamic viscosity and density of blood are considered 1060 kg/m^3 and 0.0035 Pa·s, respectively. The 6-mm-diameter arterial vessel is considered.

Using these values, we calculate the OSI, TAWSS (in Pa), and RRT (in m^2/N) over stenotic walls. Figure 11 shows the case of the single stenotic channel for different degrees of occlusion (10%–60%) at $Re = 750$. Note that a stenosis is located at $x/h = 10$. For the case of the lowest degree of stenosis (10% constriction) shown in Figure 11(A), the noticeable peak value of the OSI and RRT is observed at $x \approx 10.6h$ downstream of the constriction. It might be worth mentioning that there is also a narrow zone of high OSI at the right edge of the stenosis, which is the common location for all four channels with different degrees of occlusion. These regions of high OSI value are mainly associated with a reversal flow. In the TAWSS contour in Figure 11(A), the region of low WSS can be found close to the constriction upstream and downstream, which seem to expand with occlusion of up to 40% (see Figure 11(A)–(C)). In 20% stenotic channel shown in Figure 11(B), the peak OSI and RRT values move from $x \approx 10.6h$ to $x \approx 11.9h$. Also, an additional region of high OSI and RRT values appears upstream of the constriction. With that said, in the channel with 40% of occlusion (see Figure 11(C)), there are now multiple zones associated with high OSI and RRT values. Particularly, at the locations of $x \approx 9.15h$ and $x \approx 9.6h$, the RRT is relatively high, and the location of $x \approx 10.45h$ and further downstream $x \approx 17.15h$ are associated with very high RRT values. Among these particular locations, $x \approx 10.45h$ appears to be the most critical region for the development of atherosclerotic plaque because it is not only associated with a high value of OSI and RRT but also with low time-averaged WSS. Figure 11(D) illustrates the values of the descriptors for the channel with 60% stenosis. Several regions of high OSI values can be observed in the figure. Within some of these regions, $x \approx 9.3h$ and $x \approx 10.55h$ are associated with very high and relatively high RRT values, respectively, and both with low TAWSS. Thus, these two locations seem to be of atherogenic regions for 60% occlusion. In addition to these locations, $x \approx 11.45h$ and $x \approx 13.5h$ are associated with very high RRT and OSI values.

To compare the hemodynamics in the single and double stenotic channels, Figure 12 shows the WSS-based descriptors evaluated over the stenotic wall in the single and double stenotic channels with 50% constrictions at $Re = 750$.

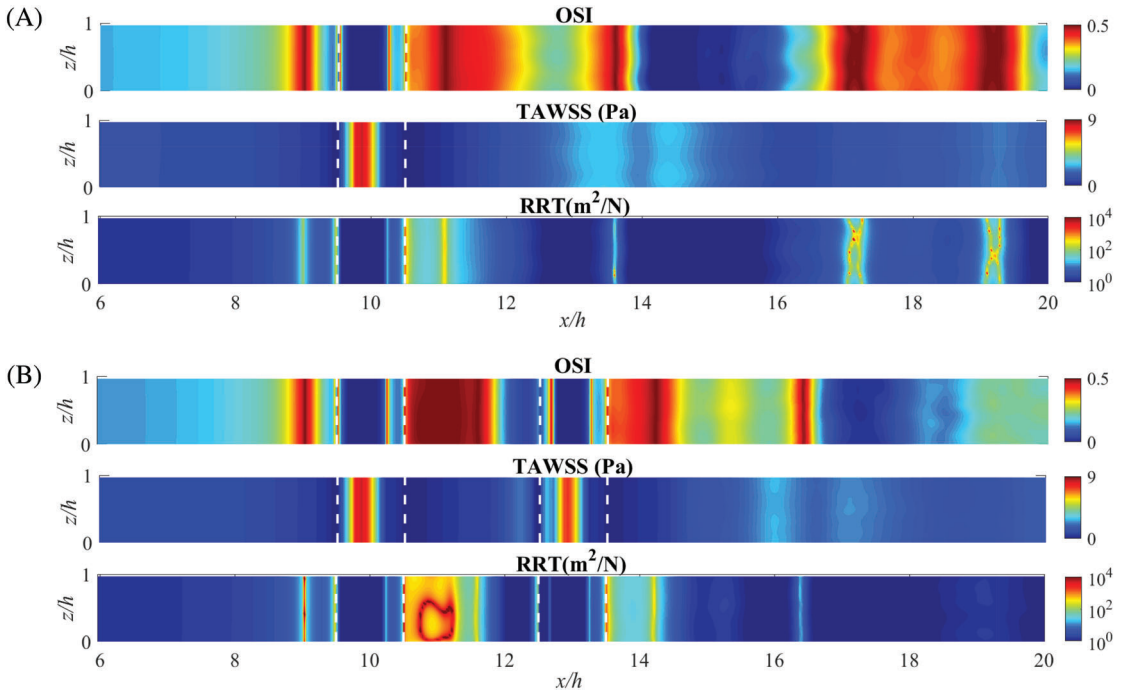

FIGURE 12 (Color online) (A) Wall shear stress-based descriptors including the time-averaged wall shear stress (TAWSS), oscillatory shear index (OSI) and relative residence time (RRT) at $Re = 750$ at (A) single and (B) double stenotic channels with 50% constrictions. The dashed lines indicate the edges of the stenoses. The centers of stenosis are located at $x/h = 10$ for the single stenotic channel and at $x/h = 10$ and 13 for the double stenotic channel

In general, an additional stenosis results in critical regions in terms of all three descriptors across the space between the stenoses in the double stenotic channel. In the interspace area of the double constricted channel in Figure 12(B), the high OSI region right after the proximal stenosis extends in x direction about $1.2h$, indicating strong oscillation of WSS at this region. The relative resident time is also seen to be high in this region. Additionally, nearly 50% of this region of high RRT and OSI values is associated with a low TAWSS. In this area, there is another low TAWSS region at the left edge of the distal stenosis $x/h \approx 9.5$, where both RRT and OSI values are relatively high. This region is seen to associate with the aforementioned strong recirculation (see Figure 7), which seems to last for the major portion of the entire pulsatile cycle. It implies that this interspace area is a potential zone for atherosclerosis progression. In addition to creating the critical interspace area, the double stenotic channel leads to a larger region of high RRT values in the immediate post-stenotic area compared to the single stenotic channel. Interestingly, the double stenotic channel shows a longer relative residence time at the location of $x \approx 9h$ than the single stenotic channel, which eventually affects the hemodynamics downstream.

4 | CONCLUSION

A computational model based on DNS coupled the IBM is developed to simulate a flow over the single and double constricted channels to study fluid dynamic and hemodynamic characteristics. This work is motivated by a great interest in the atherosclerosis-related field of research to understand the hemodynamics in the stenotic arteries based on WSS. We simulate the pulsatile flow through the three-dimensional planar channel with single and double one-sided semicircular constrictions at Reynolds numbers of 750 and 1000. For characteristic fluid and hemodynamic behaviors, we examine the instantaneous and time-averaged fluid flow and calculate the WSS-based descriptors including time-averaged WSS (TAWSS), oscillatory shear index (OSI), and relative residence time (RRT) over the channel wall with single stenosis or double stenoses. These descriptors are known to characterize and locate the regions prone to formation of atherosclerotic plaques in the channels studied. It is shown that the post-stenotic area is associated with more chaotic fluid fields, unique vortical structures, and turbulent-like characteristics. These features consequently promote the oscillatory WSS and the relative residence time of atherogenic particles and also induce more locations of low WSS, which eventually results in the critical post-stenotic locations prone to plaque formation. Moreover, the presence of two constrictions is seen to lead to further increase of the post-stenotic disturbance and the disintegration of shear layers downstream, a transition to high-intensity and broadband turbulence in the post-stenotic flow, and strengthen the characteristic recirculation zone at the beginning of the poststenotic zone. This becomes more noticeable for a higher Reynolds number of 1000. In addition, the most apparent impact of the double stenoses is the associated inter-space area, where multiple recirculations are created. This area is also seen to be highly subjected to progression of atherosclerotic plaque as it includes the regions of low and oscillatory WSS and high relative resident time. We also evaluate the effects of stenosis degree on the location of the critical region as a function of the WSS-based descriptors. In general, the higher the degree of occlusion, the larger the regions of the non-physiological ranges of the WSS properties.

Furthermore, the absorption and accumulation of LDL particles in artery walls tend to trigger many events that initiate and propagate lesion development and consequently increase atherosclerosis risk.[63] With characterizing the localized nonphysiological range of WSS-based hemodynamic parameters in a constricted flow, the current study may provide a potential location of high exposure to LDL particles. However, an explicit quantification of LDL exposure time should require a multiscale model, motivating future research.

Moving forward, the IBM-based DNS model will be updated to handle more realistic stenotic arteries with deformable and irregular shapes to simulate a highly complex FSI system. Studying the interactions between the deformable hyper-elastic vessel wall and the blood flow during the cardiac cycle is crucial as it could significantly effect the hemodynamics and the wall normal and shear stresses in the stenotic artery.

ACKNOWLEDGEMENTS

The authors gratefully acknowledge financial support from the Collaboration Initiative at the University of Nebraska and, in part, from the National Science Foundation through Grant No. CBET-1936065 (Particulate and Multiphase Processes program). The authors would also like to thank S. Ryu & T. Wei at the University of Nebraska-Lincoln and X. Liu & Y. Chatzizisis at the University of Nebraska Medical Center for fruitful discussions. This work was completed utilizing the Holland Computing Center of the University of Nebraska, which receives support from the Nebraska Research Initiative.

CONFLICT OF INTEREST

The authors declare no conflict of interest regarding the publication of this article.

PEER REVIEW

The peer review history for this article is available at https://publons.com/publon/10.1002/eng2.12444.

DATA AVAILABILITY STATEMENT

The data that support the findings of this study are available from the corresponding author upon reasonable request.

ORCID

Jae Sung Park https://orcid.org/0000-0002-7966-1164

REFERENCES

1. Ross R. Atherosclerosis. an inflammatory disease. *N Engl J Med*. 1999;340(2):115-126.
2. Stein P, Walburn F, Sabbah H. Turbulent stresses in the region of aortic and pulmonary valves; 1982.
3. Libby P. Inflammation in atherosclerosis. *Arterioscler Thromb Vasc Biol*. 2012;32(9):2045-2051.
4. Westein E, van der Meer AD, Kuijpers MJ, Frimat JP, van den Berg A, Heemskerk JW. Atherosclerotic geometries exacerbate pathological thrombus formation poststenosis in a von Willebrand factor-dependent manner. *Proc Natl Acad Sci*. 2013;110(4):1357-1362.
5. Malek AM, Alper SL, Izumo S. Hemodynamic shear stress and its role in atherosclerosis. *JAMA*. 1999;282(21):2035-2042.
6. Mittal R, Simmons S, Najjar F. Numerical study of pulsatile flow in a constricted channel. *J Fluid Mech*. 2003;485:337-378.
7. Varghese SS, Frankel SH, Fischer PF. Direct numerical simulation of stenotic flows. Part 2. pulsatile flow. *J Fluid Mech*. 2007;582:281-318.
8. Molla MM, Wang BC, Kuhn DC. Numerical study of pulsatile channel flows undergoing transition triggered by a modelled stenosis. *Phys Fluids*. 2012;24(12):121901.
9. Himburg HA, Grzybowski DM, Hazel AL, LaMack JA, Li XM, Friedman MH. Spatial comparison between wall shear stress measures and porcine arterial endothelial permeability. *Am J Phys Heart Circ Phys*. 2004;286(5):H1916-H1922.
10. Ziegler T, Bouzourene K, Harrison VJ, Brunner HR, Hayoz D. Influence of oscillatory and unidirectional flow environments on the expression of endothelin and nitric oxide synthase in cultured endothelial cells. *Arterioscler Thromb Vasc Biol*. 1998;18(5):686-692.
11. Pedrigi RM, Mehta VV, Bovens SM, et al. Influence of shear stress magnitude and direction on atherosclerotic plaque composition. *Royal Soc Open Sci*. 2016;3(10):160588.
12. Glagov S, Zarins C, Giddens DP, Ku DN. Hemodynamics and atherosclerosis. Insights and perspectives gained from studies of human arteries. *Arch Pathol Lab Med*. 1988;112(10):1018-1031.
13. Lees RS, Dewey CF. Phonoangiography: a new noninvasive diagnostic method for studying arterial disease. *Proc Natl Acad Sci*. 1970;67(2):935-942.
14. Giddens DP, Zarins CK, Glagov S. The role of fluid mechanics in the localization and detection of atherosclerosis. *J Biomech Eng*. 1993;115(4B):588-594.
15. Zhu C, Seo JH, Mittal R. Computational modeling and analysis of murmurs generated by modeled aortic stenoses. *J Biomech Eng*. 2019;141(4):041007.
16. Timmins LH, Molony DS, Eshtehardi P, et al. Oscillatory wall shear stress is a dominant flow characteristic affecting lesion progression patterns and plaque vulnerability in patients with coronary artery disease. *J R Soc Interface*. 2017;14(127):20160972.
17. Shaaban AM, Duerinckx AJ. Wall shear stress and early atherosclerosis: a review. *Am J Roentgenol*. 2000;174(6):1657-1665.
18. Sabbah HN, Stein PD. Hemodynamics of multiple versus single 50 percent coronary arterial stenoses. *Am J Cardiol*. 1982;50(2):276-280.
19. Vlachopoulos C, O'Rourke M, Nichols WW. *McDonald's Blood Flow in Arteries: Theoretical, Experimental and Clinical Principles*. CRC Press; 2011.
20. Seeley BD, Young DF. Effect of geometry on pressure losses across models of arterial stenoses. *J Biomech*. 1976;9(7):439-448.
21. Bernad SI, Bernad ES, Craina M, Sargan I, Totoran A, Brisan C. Particle depositions and related hemodynamic parameters in the multiple stenosed right coronary artery. *J Clin Med Res*. 2012;4(3):177.
22. Lee T, Liao W, Low H. Numerical study of physiological turbulent flows through series arterial stenoses. *Int J Numer Methods Fluids*. 2004;46(3):315-344.
23. Varghese SS, Frankel SH, Fischer PF. Direct numerical simulation of stenotic flows. Part 1. steady flow. *J Fluid Mech*. 2007;582:253-280.
24. Blackburn HM, Sherwin SJ, Barkley D. Convective instability and transient growth in steady and pulsatile stenotic flows. *J Fluid Mech*. 2008;607:267-277.
25. Beratlis N, Balaras E, Parvinian B, Kiger K. A numerical and experimental investigation of transitional pulsatile flow in a stenosed channel. *J Biomech Eng*. 2005;127(7):1147-1157.
26. Mittal R, Simmons S, Udaykumar H. Application of large-eddy simulation to the study of pulsatile flow in a modeled arterial stenosis. *J Biomech Eng*. 2001;123(4):325-332.
27. Molla MM, Paul M. LES of non-Newtonian physiological blood flow in a model of arterial stenosis. *Med Eng Phys*. 2012;34(8):1079-1087.
28. Peskin CS. Flow patterns around heart valves: a numerical method. *J Comput Phys*. 1972;10:252-271.

29. Fadlun E, Verzicco R, Orlandi P, Mohd-Yusof J. Combined immersed-boundary finite-difference methods for three-dimensional complex flow simulations. *J Comput Phys*. 2000;161(1):35-60.
30. Kim J, Kim D, Choi H. An immersed-boundary finite-volume method for simulations of flow in complex geometries. *J Comput Phys*. 2001;171(1):132-150.
31. Mustapha N, Mandal PK, Johnston PR, Amin N. A numerical simulation of unsteady blood flow through multi-irregular arterial stenoses. *Appl Math Model*. 2010;34(6):1559-1573.
32. Yakhot A, Grinberg L, Nikitin N. Modeling rough stenoses by an immersed-boundary method. *J Biomech*. 2005;38(5):1115-1127.
33. Mittal R, Dong H, Bozkurttas M, Najjar F, Vargas A, Von Loebbecke A. A versatile sharp interface immersed boundary method for incompressible flows with complex boundaries. *J Comput Phys*. 2008;227(10):4825-4852.
34. Seo JH, Bakhshaee H, Garreau G, et al. A method for the computational modeling of the physics of heart murmurs. *J Comput Phys*. 2017;336:546-568.
35. Kan K, Yang Z, Lyu P, Zheng Y, Shen L. Numerical study of turbulent flow past a rotating axial-flow pump based on a level-set immersed boundary method. *Renew Energy*. 2021;168:960-971. https://doi.org/10.1016/j.renene.2020.12.103
36. Roy S, De A, Balaras E. *Immersed Boundary Method: Development and Applications*. Springer Nature; 2020.
37. Wang J, Paritala PK, Mendieta JB, et al. Optical coherence tomography-based patient-specific coronary artery reconstruction and fluid–structure interaction simulation. *Biomech Model Mechanobiol*. 2020;19(1):7-20.
38. Lopes D, Puga H, Teixeira J, Teixeira S. Influence of arterial mechanical properties on carotid blood flow: comparison of CFD and FSI studies. *Int J Mech Sci*. 2019;160:209-218. https://doi.org/10.1016/j.ijmecsci.2019.06.029
39. Liu J, Yang W, Lan IS, Marsden AL. Fluid-structure interaction modeling of blood flow in the pulmonary arteries using the unified continuum and variational multiscale formulation. *Mech Res Commun*. 2020;107:103556. https://doi.org/10.1016/j.mechrescom.2020.103556
40. Bäumler K, Vedula V, Sailer AM, et al. Fluid–structure interaction simulations of patient-specific aortic dissection. *Biomech Model Mechanobiol*. 2020;19(5):1607-1628.
41. Lopes D, Puga H, Teixeira J, Lima R. Blood flow simulations in patient-specific geometries of the carotid artery: a systematic review. *J Biomech*. 2020;111:110019. https://doi.org/10.1016/j.jbiomech.2020.110019
42. Liu J, Marsden AL. A unified continuum and variational multiscale formulation for fluids, solids, and fluid–structure interaction. *Comput Methods Appl Mech Eng*. 2018;337:549-597.
43. Chen Y, Yang X, Iskander AJ, Wang P. On the flow characteristics in different carotid arteries. *Phys Fluids*. 2020;32(10):101902. https://doi.org/10.1063/5.0022092
44. Griffith MD, Leweke T, Thompson MC, Hourigan K. Effect of small asymmetries on axisymmetric stenotic flow. *J Fluid Mech*. 2013;721:R1. https://doi.org/10.1017/jfm.2013.109
45. Tutty O. Pulsatile flow in a constricted channel. *J Biomech Eng*. 1992;114:50-54.
46. Griffith MD, Thompson MC, Leweke T, Hourigan K, Anderson WP. Wake behaviour and instability of flow through a partially blocked channel. *J Fluid Mech*. 2007;582:319-340.
47. Ahmed SA, Giddens DP. Flow disturbance measurements through a constricted tube at moderate Reynolds numbers. *J Biomech*. 1983;16(12):955-963.
48. Pedley T. *The Fluid Mechanics of Large Blood Vessels*. Cambridge University Press; 1980.
49. Lieber BB, Giddens DP. Post-stenotic core flow behavior in pulsatile flow and its effects on wall shear stress. *J Biomech*. 1990;23(6):597-605.
50. Kim BM, Corcoran WH. Experimental measurements of turbulence spectra distal to stenoses. *J Biomech*. 1974;7(4):335-342. https://doi.org/10.1016/0021-9290(74)90028-1
51. Lu P, Gross D, Hwang N. Intravascular pressure and velocity fluctuations in pulmonic arterial stenosis. *J Biomech*. 1980;13(3):291-300. https://doi.org/10.1016/0021-9290(80)90371-1
52. Pandey R, Kumar M, Majdoubi J, Rahimi-Gorji M, Srivastav VK. A review study on blood in human coronary artery: numerical approach. *Comput Methods Prog Biomed*. 2020;187:105243.
53. De Wilde D, Trachet B, De Meyer GR, Segers P. Shear stress metrics and their relation to atherosclerosis: an in vivo follow-up study in atherosclerotic mice. *Ann Biomed Eng*. 2016;44(8):2327-2338.
54. Malek AM, Izumo S. Control of endothelial cell gene expression by flow. *J Biomech*. 1995;28(12):1515-1528.
55. Davies PF. Flow-mediated endothelial mechanotransduction. *Physiol Rev*. 1995;75(3):519-560.
56. Fung YC. *Biomechanics: Circulation*. Springer Science & Business Media; 2013.
57. Schwartz C, Valente A, Sprague EA, Kelley J, Nerem R. The pathogenesis of atherosclerosis: an overview. *Clin Cardiol*. 1991;14(S1):1-16.
58. Himburg HA, Friedman MH. Correspondence of low mean shear and high harmonic content in the porcine iliac arteries. *J Biomech Eng*. 2006;128(6):852-856.
59. Lee SW, Antiga L, Steinman DA. Correlations among indicators of disturbed flow at the normal carotid bifurcation. *J Biomech Eng*. 2009;131(6):061013.
60. Suess T, Anderson J, Danielson L, et al. Examination of near-wall hemodynamic parameters in the renal bridging stent of various stent graft configurations for repairing visceral branched aortic aneurysms. *J Vasc Surg*. 2016;64(3):788-796.
61. Pinto SIS, Campos JBLM. Numerical study of wall shear stress-based descriptors in the human left coronary artery. *Comput Methods Biomech Biomed Eng*. 2016;19(13):1443-1455.
62. Ahmed SA, Giddens DP. Pulsatile poststenotic flow studies with laser Doppler anemometry. *J Biomech*. 1984;17(9):695-705.

63. Borén J, Chapman MJ, Krauss RM, et al. Low-density lipoproteins cause atherosclerotic cardiovascular disease: pathophysiological, genetic, and therapeutic insights: a consensus statement from the European atherosclerosis society consensus panel. *Eur Heart J*. 2020;41(24):2313-2330. https://doi.org/10.1093/eurheartj/ehz962

SUPPORTING INFORMATION

Additional supporting information may be found online in the Supporting Information section at the end of this article.

How to cite this article: Mirfendereski S, Park JS. Direct numerical simulation of a pulsatile flow in a stenotic channel using immersed boundary method. *Engineering Reports*. 2021;e12444. https://doi.org/10.1002/eng2.12444